18TH LISBON 2016
INTERNATIONAL SYMPOSIUM
ON APPLICATIONS OF LASER AND IMAGING TECHNIQUES TO FLUID MECHANICS
FROM 4 TO 7 OF JULY

PROCEEDINGS

OF THE

18th INTERNATIONAL

SYMPOSIUM ON

APPLICATION OF

LASER AND IMAGING

TECHNIQUES TO

FLUID MECHANICS

Statistical Characterization of Helium-Filled Soap Bubbles Tracing Fidelity for PIV

Koen L.L. Morias[1], Giuseppe C.A. Caridi[1,*], Andrea Sciacchitano[1], Fulvio Scarano[1]
1: Dept. of Aerospace Engineering, Delft University of Technology, Delft, The Netherlands
* Correspondent author: g.caridi@tudelft.nl

Keywords: Large-scale PIV, tracing fidelity, Helium-filled soap bubbles

ABSTRACT

The present work follows a previous study on the aerodynamic characterization of helium-filled soap bubbles (HFSBs) for large-scale PIV measurements. HFSBs were found to yield, on average, a time response of about 10μs. However, the response of each individual tracer remained to be ascertained, which is the topic of the present study. The velocity of the bubbles in the stagnation region ahead of a circular cylinder is evaluated by the PTV technique. The results are compared with micro-size fog droplets taken as reference. The tracking error of individual trajectories is assessed by statistical analysis of the relative slip between the bubble and the airflow. The instantaneous particle relaxation time is retrieved from the ratio between slip velocity and local acceleration. Additional information on the bubble instantaneous properties is taken by inferring the diameter from the distance between the glare points. The results are discussed and related to the differences observed in the bubbling and jetting regimes for bubble production. Finally, the HFSBs relative density to the air is estimated using a modified Stokes drag law.

1. Introduction

Since the introduction of Tomographic Particle Image Velocimetry (Tomo-PIV), the measurement volume has been recognized as a major bottleneck due to the limitation of laser pulse energy and the constraints on imaging depth of focus (Scarano 2013). The use of lasers with pulse energy up to 1 J has marginally increased the volume with respect to the first experiment conducted by Elsinga et al. (2006), where the velocity was measured in a domain of $3.5\times3.5\times0.7$ cm^3. Instead, experiments in water flows could be conducted at significant larger size by using large neutrally buoyant tracers. The little energy scattered by micro-size tracers can be considered as the main limitation preventing the upscale of Tomo-PIV and its deployment for industrial aerodynamics. The use of sub-millimeter helium-filled soap bubbles (HFSBs) as tracer particles has shown to overcome this limitation. With a diameter (300-500 μm) two orders of magnitude larger than the conventional seeding particles, the amount of scattered light enables the measurement over a measurement volume several orders of magnitude larger (Caridi et al. 2015).

The first analysis on the tracking fidelity of HFSBs was performed by Kerho and Bragg (1994) in the stagnation region of a NACA0012 airfoil. Bubbles with diameter varying between 1 and 5 mm were used. However, the use of a device filtering heavier bubbles caused the average density of bubbles to become slightly lighter-than-air causing a marked departure from the streamlines of the airflow. The conclusion was that HFSBs did not qualify for quantitative measurements in aerodynamics. Bosbach et al. (2009) introduced a novel bubble generator developed by the German Aerospace Center (DLR) capable of producing bubbles of 0.2 to 0.6 mm with a high production rate (50,000 bubbles/ s). Planar PIV measurements on the mixed convective flow in a full scale airplane cabin mock-up (measurement domain of 7 m^2) demonstrated their effectiveness as flow tracers. A large-scale tomographic application is reported by Kuhn et al. (2011) addressing the three-dimensional flow field in a rectangular convective cell over a volume of 75×45×16.5 cm^3.

The tracing fidelity of these bubbles has been studied recently by Scarano et al. (2015). The bubbles velocity in the stagnation region of a cylinder was compared with that of micro-size droplets, taken as reference for the airflow. HFSBs can be produced approaching neutral buoyancy and exhibiting a mean relaxation time of about 10 μs. Furthermore, the authors demonstrated the potential to employ these tracers for large-scale time-resolved tomographic PIV with a measurement in a volume of 20×20×12 cm^3 in the wake of a cylinder of 4.5 cm. Later, Caridi et al. (2015) developed a dedicated seeding system to increase the concentration of tracers for large-scale experiments in wind tunnels reaching a measurement volume of 16,000 cm . The use of HFSBs for large-scale experiments is also documented in the work of Schneiders et al. (2015) who used the bubbles to reconstruct the instantaneous flow pressure in the wake of a cylinder-flat plate by time-resolved Tomo-PIV measurements.

Some questions remain open concerning the aerodynamic behaviour of HFSBs. First, Scarano et al. (2015) report only the ensemble average relaxation time of the HFSBs. It is not known to what extent individual bubbles depart from the mean. This aspect is of primary importance to validate the use of HFSBs for velocity fluctuations and turbulent statistics. Furthermore, the results reported on the tracing behaviour of the bubbles rely on the hypothesis of Stokes flow theory, which is only valid at Reynolds number well below unity. The latter is defined as:

$$\mathrm{Re}_p = \frac{\rho_f \left| \boldsymbol{u}_f - \boldsymbol{u}_p \right| d_p}{\mu_f} \qquad (1)$$

where $\boldsymbol{u}_p$ and d_p and are the particle velocity and diameter, respectively. The symbol $\boldsymbol{u}_f$ refers to the flow velocity. The difference between particle velocity and fluid velocity is referred to as *slip velocity*. Density and dynamic viscosity of the fluid are expressed by ρ_f and μ_f, respectively. When

the specific density of a bubble $\bar{\rho}$ (ratio of bubble density over fluid density) deviates from unity and the diameter increases, a finite slip velocity arises and the assumption $Re_p<<1$ may no longer be valid. In this condition, the bubble motion relative to the air is not in the Stokes flow regime and the equation of motion reads as (Mei, 1996):

$$\frac{4}{3}\pi a^3 \rho_p \frac{d\boldsymbol{u}_p}{dt} = 6\pi\mu_f a\Phi\left(\mathrm{Re}_p\right)\left(\boldsymbol{u}_f - \boldsymbol{u}_p\right) + \frac{4}{3}\pi a^3 \rho_f \frac{D\boldsymbol{u}_f}{Dt} \qquad (2)$$

In Equation (2), gravity force, added-mass force, time-history force and Magnus force have been neglected. The term on the left-hand side is the particle inertia. The right-hand side contains the quasi-steady drag force and the pressure force. The terms are expressed in function of particle radius *a*. The temporal derivative D/ Dt is expressed following a fluid element, whereas d/ dt is considered along the particle path. The quasi-steady drag force differs from the viscous Stokes drag by an empirical correction factor $\phi(Re_p)\geq 1$, which accounts for the finite particle Reynolds number. An overview of the available correction factors and their accuracy is given by Clift et al. (1978).

The present work aims at characterizing statistically the tracing fidelity of HFSBs in PIV experiments. The tracing capability of the bubbles is studied considering the statistical distribution of the bubbles' diameter, slip velocity, relaxation time and density. The analysis will account not only for the viscous Stokes drag, but also for quasi-steady drag at finite Re_p. The contribution of the latter will be evaluated in the slip velocity and particle response time.

An experiment is performed at a spatial resolution such to determine simultaneously the bubbles trajectory and their diameter. Based on the relaxation time, the study will determine the tracing fidelity expected from individual bubbles and its dependence upon the bubble generation regime.

2. Experimental Setup

The experiment is conducted in the W-tunnel, an open-jet open-return facility of the Aerodynamics Laboratories of TU Delft. The tunnel has a test section of 40×40 cm with a free-stream turbulence level of approximately 0.5% at 20 m/ s.

The model is a circular cylinder with a diameter of 40 mm. A splitter plate, with a length of 7 cylinder diameters and a thickness of 2 mm, is attached to the aft of the cylinder preventing the von Kármán vortex shedding and the resulting fluctuations of the stagnation point. Experiments are conducted at freestream velocity V_∞=20 m/ s. The stagnation region in front of the cylinder

features an irrotational, steady, two-dimensional, incompressible flow, which can be accurately modelled with potential flow theory. Figure 1-right illustrates the experimental setup.

The imaging system consists of a Photron Fast Cam SA1 camera (CMOS, 1,024×1,024 pixels, 12-bit, pixel pitch 20 μm). The camera is equipped with a 105 mm Nikkor objective with aperture settings of f/ 5.6 (for measurements with fog droplets) and f/ 16 (for measurements with HFSBs). The sensor is cropped to 704×336 pixels. The field of view is 3.41×1.63 cm , yielding an optical magnification of 0.41. The illumination is provided by a Quantronix Darwin-Duo Nd:YLF laser with nominal pulse energy of 2×25 mJ at 1 kHz.

The reference velocity field is obtained by PIV measurements with micro-size fog droplets, generated by a SAFEX Twin Fog smoke generator (median particle diameter of 1 μm). A set of 3,000 double-frame images is acquired at a frequency of 250 Hz with a time separation of 38 μs. Image pre-processing and cross-correlation are performed with LaVision Davis 8.2. The final interrogation window size is 16×16 pixels and the overlap is 75%. This results in a vector pitch of approximately 0.2 mm.

For the HFSBs measurements, 20,000 single-frame images are acquired at an acquisition frequency of 20,000 Hz. The experimental setup follows that used for the fog measurements. A single LaVision bubble generator (production rate of 50,000 bubbles/ s) is installed in the settling chamber of the wind tunnel inside a NACA0012 airfoil (chord length of 12 cm) to minimize the aerodynamic intrusiveness of the seeding probe (Figure 1-left). The bubble diameter and density is controlled by varying the pressure of the bubble fluid solution (BFS) mixture, helium and air flow through the supply unit of the bubble generator. For a detailed description of the working principle of the bubble generator, the reader is referred to Bosbach et al. (2009).

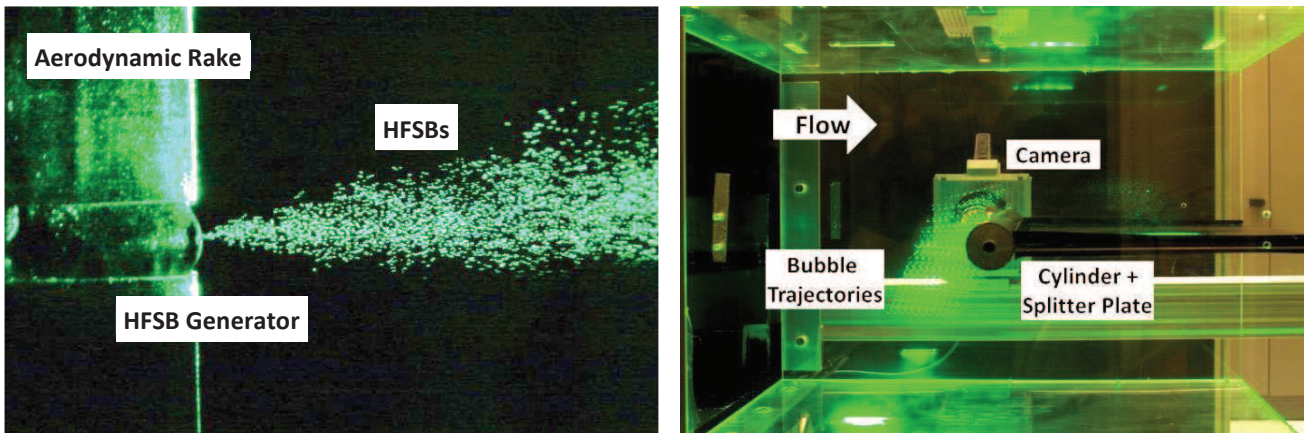

Fig. 1 Experimental setup. Left: bubble generator in settling chamber. Right: test section.

3. Methodology

3.1 Velocity and Acceleration

Velocity and acceleration measurements of the HFSBs are carried out using the Particle Tracking Velocimetry (PTV) technique. The particle-tracking algorithm is based on that of Malik et al. (1993). Sub-pixel accuracy is applied by fitting a Gaussian intensity through the intensity peaks of the image particles. The position of the tracer along its trajectory is regularized fitting the measured values with a third order polynomial. Each fit makes use of seventeen consecutive images. The first time-derivative of the polynomial yields the velocity and the second time-derivative gives the Lagrangian acceleration at the particle location. The reference flow velocity is obtained via a cross-correlation of the PIV images obtained with fog droplets as tracers. A comparison of the velocity and acceleration along the stagnation line is performed, where the fluid and the tracers therein undergo one-dimensional deceleration. For the HFSBs, the mean velocity and acceleration of all the bubbles are computed by averaging the instantaneous values within a box of 24 pixels height (symmetric around the stagnation streamline) and 15 pixels streamwise length. The reference velocity from fog droplets is interpolated to the bubble position and averaged within the same control volume as that used for HFSBs. The Lagrangian acceleration of the flow is defined as:

$$\frac{D\boldsymbol{u}}{Dt} = \frac{\partial \boldsymbol{u}}{\partial t} + \boldsymbol{u} \cdot \nabla \boldsymbol{u} \qquad (3)$$

where the first term of the right-hand side is zero due to the steady flow field. Thus, the Lagrangian acceleration can be evaluated solely by the convective term $\boldsymbol{u} \cdot \nabla \boldsymbol{u}$. The velocity gradient in Equation (3) is obtained with a second order central finite difference scheme.

3.2 Bubble Diameter

Each bubble is visible through two glare points (van de Hulst and Wang, 1992). In the present experiment the viewing axis is perpendicular to the illumination direction. Therefore, the relation between the bubble diameter d_p and the distance between the image of the glare points d_G reads as:

$$d_p = \sqrt{2} d_G \qquad (4)$$

3.3 Tracing Fidelity

The particle relaxation time τ_p can be computed as:

$$\tau_p = \left| \frac{\boldsymbol{u}_p - \boldsymbol{u}_f}{\boldsymbol{u} \cdot \nabla \boldsymbol{u}} \right| \qquad (5)$$

When the assumption of Stokes flow regime does not hold strictly, the relaxation time is no longer a constant, but it varies in the flow field depending on the local acceleration and associated slip velocity. An expression of the relaxation time that includes an empirical drag correction factor is given below. The correction factor used in this work is the one by Schiller and Naumann (1933), which expands the range of validity to $\mathrm{Re}_p < 800$:

$$\tau_p = \frac{d_p^2}{18} \frac{\left| \rho_p - \rho_f \right|}{\mu_f} \frac{1}{\Phi\left(\mathrm{Re}_p\right)} \qquad (6)$$

The above expressions are true under the assumption that the fluid acceleration equals the particle acceleration and that gravity and history force can be neglected.

3.4 Bubble density

The bubble density is retrieved by solving Equation (6) for ρ_p. The bubble diameter is measured as described in section 3.2. The slip velocity and thus the particle Reynolds number is determined by calculating the difference between the bubble velocity and the reference velocity field (section 3.1). The particle relaxation time is measured as given in Equation (5). Finally, the density of the surrounding fluid air is calculated using the perfect gas law (pressure and temperature were recorded during the laboratory experiments).

4. Bubble formation regimes

The generation process of HFSBs has direct effects on PIV measurements where the bubbles are used as tracers. As discussed by Melling (1997), diameter and density of the seeding particles define their tracking capabilities. As a consequence, tracers with monodisperse distribution in size and density are preferable for more accurate measurements.

HFSBs are generated with an orifice-type nozzle, as described by Bosbach et al. (2009). The design of the present nozzle was developed in order to produce bubbles in a so-called *co-flow* configuration, also commonly used for air bubble production in water flows (Sevilla et al. 2005a). Sevilla et al. (2005b) and Gañán-Calvo et al. (2006) discussed the importance of the velocity ratio between the co-flowing fluids for a stable and continuous bubble production. Two different formation regimes were identified: *bubbling* and *jetting*. The latter is characterized by a long cylindrical ligament of the discrete phase that breaks up far from the exit of the generator. This

results in an aperiodic and polydisperse bubble production. Conversely, the *bubbling* regime features a fairly periodic and stable formation of the bubbles at the exit of the nozzle.

In the present work, the HFSB generator shows similar working regimes to those mentioned above. The details of HFSB formation at the exit of the nozzle are inspected with high-speed shadowgraphy at 90 kHz, with continuous illumination. The results in Figure 2 illustrate an example of the stable *bubbling* regime with rather monodisperse size distribution (Figure 2a). The visualizations also reveal the formation of small droplets at the moment of detachment, either inside or outside the bubble. Although irrelevant for the bubble diameter, this phenomenon may affect the dispersion of bubble weight. In the observed *bubbling* regime, HFSBs are ejected with a velocity of 20 m/ s and with an average separation distance of 440 µm between each other; hence, the production rate is estimated to be approximately 50,000 bubbles per second.

When the bubble generator operates in the *jetting* regime, a quasi-cylindrical interface of BFS protrudes from the exit of the nozzle. It was observed that the cylindrical film is affected by large scale fluctuations and occasionally breaks up into bubbles far from the orifice. The resulting bubbles are characterized by a broader distribution in diameter, as illustrated in Figure 2b.

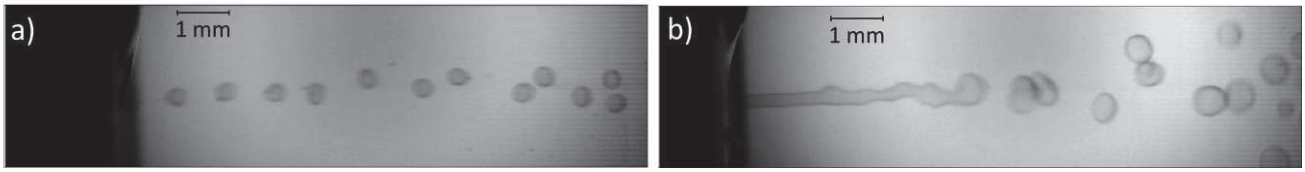

Fig. 2 High speed visualization of HFSB production in bubbling (a) and jetting regime (b).

5. Experimental Results

Neutrally buoyant helium-filled soap bubbles are generated suppling flow rates of q_{bfs}=4.78 ml/ h, q_{He}=4.83 l/ h and q_{sa}=115.30 l/ h, where *bfs*, *He* and *sa* indicate bubble fluid solution, helium and secondary air, respectively. The heavier-than-air bubbles are generated with air instead of Helium inside the bubbles.

The mean velocity and acceleration profiles of neutrally buoyant and heavier-than-air bubbles on the stagnation streamline at a freestream velocity of 20 m/ s are illustrated in Figure 3. The results are shown with the reference data obtained by PIV measurements with fog droplets. The uncertainty is illustrated with error bars that represent the standard deviations of the measurements. Figure 3 shows that the mean velocity and acceleration profile of the neutrally buoyant bubbles are in agreement with those of the fog measurements. The heavier-than-air bubbles profile exhibits the expected offset, indicating a delayed response to the decelerating flow and confirming the observations of Scarano et al. (2015). This delay is also clearly visible in the acceleration profile, where heavier-than-air bubbles exhibit lower acceleration for $x/D < -0.7$.

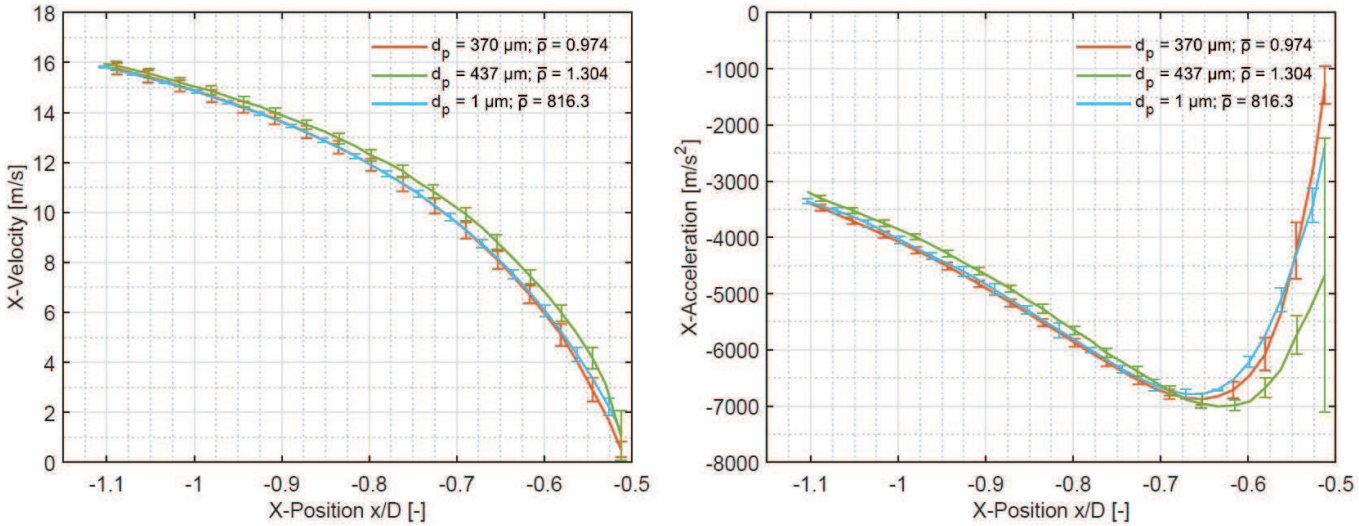

Fig. 3 Mean velocity (left) and acceleration (right) profiles on the stagnation streamline ahead the cylinder.

Largely heavier-than-air (air-filled) soap bubbles are considered first, having a specific density of about 1.3. The slip velocity and relaxation time of these bubbles are showed in Figure 4. Since the bubble velocity and acceleration are determined by means of PTV, they feature low measurement uncertainty. Random measurement errors on the bubble position are strongly reduced by fitting a third-order polynomial through the series of seventeen data points. The reference velocity field is computed as the time-average of 3,000 instantaneous uncorrelated velocity fields. The turbulence intensity of the wind tunnel is measured to be 0.5% at a freestream velocity of 20 m/ s. Since the bubble recordings and the fog droplet measurements are not made simultaneously, velocity differences up to ±0.1 m/ s can occur that are not due the aerodynamic behaviour of the bubbles, but solely to the freestream turbulence intensity. This uncertainty in the slip velocity calculation is indicated by black dashed lines in Figure 4. The light-blue dots represent individual bubble recordings, while the red line is the mean of all recordings and the error bars indicate one standard deviation of the distribution.

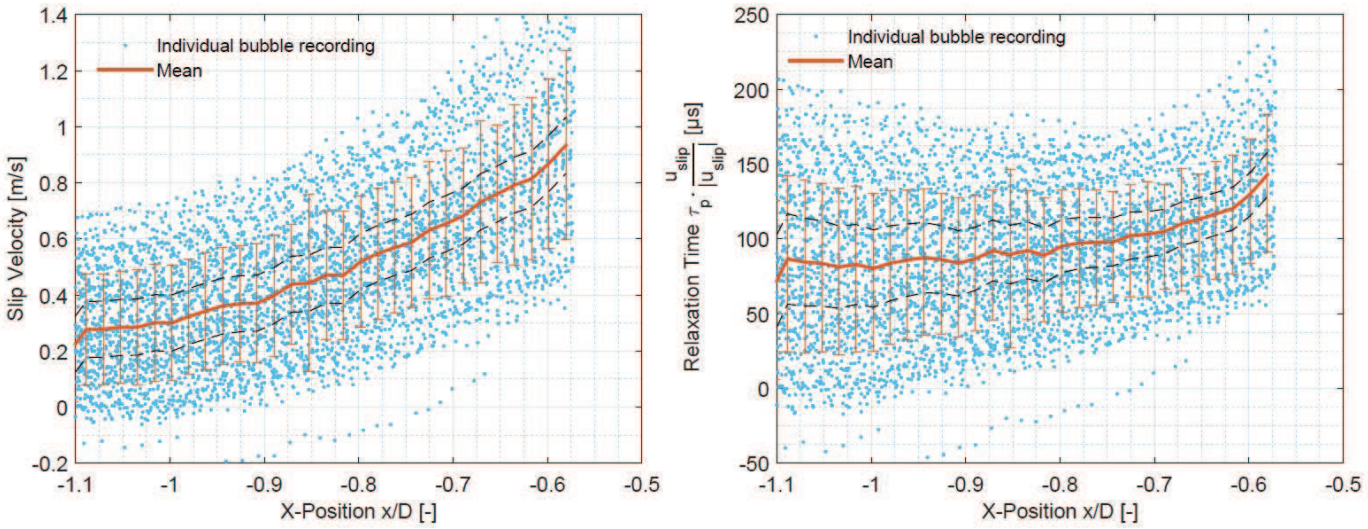

Fig. 4 Slip velocity (left) and relaxation time (right) of individual bubbles on the stagnation line of the cylinder for heavier-than-air air-filled soap bubbles. Black dashed lines indicate the uncertainty due to the freestream turbulence intensity.

In the range x/ D=[-1.1 -0.7], the acceleration approximately doubles (see Figure 3-right). Since the correction factor Φ depends on the particle Reynolds number less than linearly (Schiller and Neumann, 1933), the relaxation time can be assumed constant for small variations of the slip velocity. Assuming a constant relaxation time τ_p, also the slip velocity is expected to double. The results of Figure 4-left show an approximately linear increase of the slip velocity. While the mean value of u_{slip} doubles in the considered x/ D range, the standard deviation instead has a smaller increase. This result is ascribed to the slight overestimation of the slip velocity due to the effect of freestream turbulence. This effect is larger away from the cylinder (x/ D < -0.9), where the slip velocity is expected to be lower. For the same reason, the standard deviation of the relaxation time is probably overestimated when computed far away from the cylinder (see Figure 4-right).
The results are further analysed in the interval x/ D=[-0.75 -0.65], where the flow deceleration is the strongest, resulting in the largest slip velocity and the lowest relative influence of freestream turbulence intensity. Here the average slip velocity is approximately 0.7 m/ s with a standard deviation of 0.26 m/ s, giving a mean relaxation time of approximately 98 µs with a standard deviation of 38 µs. This indicates the poor tracing fidelity of air-filled soap bubbles and further confirms the need of Helium as filling gas to counterbalance the weight of the soap film.
The slip velocity and relaxation time of nearly neutrally buoyant HFSBs are analysed in Figure 5. Those bubbles have a specific density of about 0.97.

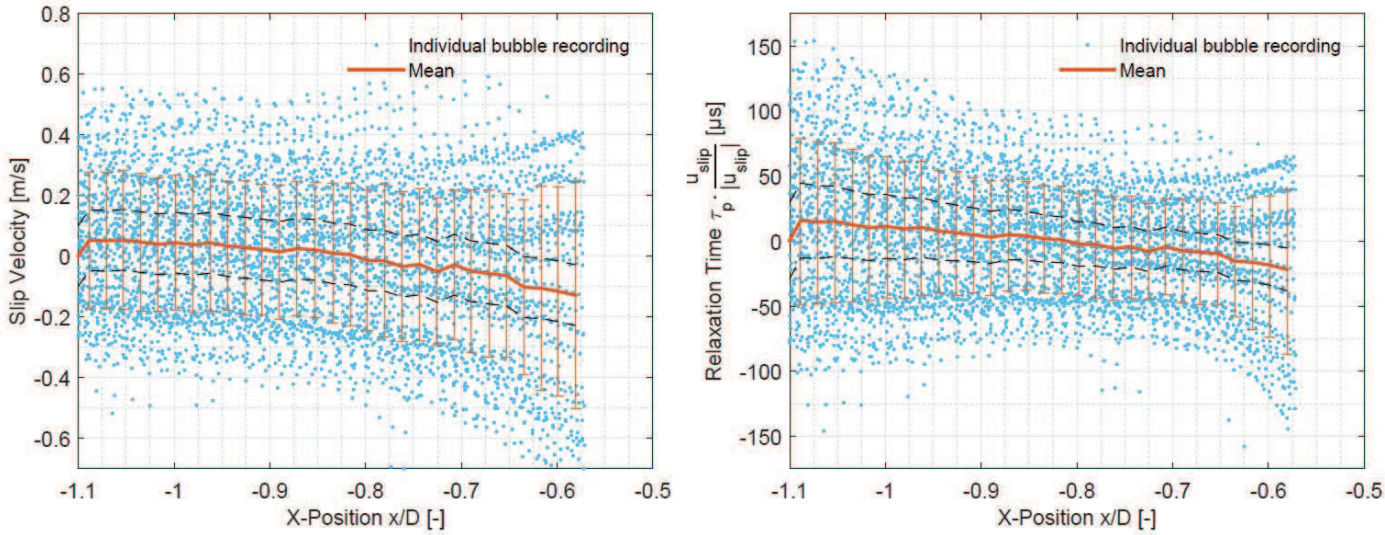

Fig. 5 Slip velocity (left) and relaxation time (right) of individual bubbles on the stagnation line of the cylinder for neutrally buoyant helium-filled soap bubbles. Black dashed lines indicate the uncertainty due to the freestream turbulence intensity.

The mean slip velocity is approximately zero for x/ D < -0.9 and slightly increases approaching the cylinder. The uncertainty due to the turbulence intensity is again indicated with black dashed lines. The magnitude of the slip velocity and the uncertainty due to the turbulence intensity are of the same order. For the same reason as before, the results are analysed in the interval x/ D=[-0.75 -0.65]. The mean slip velocity is around 0.05 m/ s with a standard deviation of 0.25 m/ s, yielding a mean relaxation time of less than 10 µs, with a more significant standard deviation of approximately 40 µs. The relaxation time in Figure 5-right is multiplied by the sign of the slip velocity. As a result, lighter than air HFSBs exhibit a negative response.

Combining the latter information with the measurement of the bubble diameter, it is possible to determine the bubble density from the definition of the relaxation time (see Section 3.4).

As depicted in Figure 6-left, the statistical distribution of the measured bubble diameter is approximately Gaussian. The average bubble diameter is 370 µm. This corresponds to an average glare point distance of 7.7 pixels. The standard deviation of the distribution is 16 µm or 0.33 pixels. Therefore the distribution is monodisperse, indicating that the nozzle operates in the *bubbling* regime and produces bubbles within 5% variations in diameter. The uncertainty of the bubble diameter is determined by dividing the standard deviation of the diameters of all the recordings of each bubble by the square root of the number of recordings of that bubble. The histogram of the diameter measurement uncertainty in Figure 6-right approximates a Poisson distribution with its peak at 2.6 µm or 0.054 pixels. Hence, the measurement uncertainty is less than 1 % of the bubble diameter. As a result, the measured 5% variation in diameter showed in Figure 6-left is due to a bubble production process that is not perfectly repeatable.

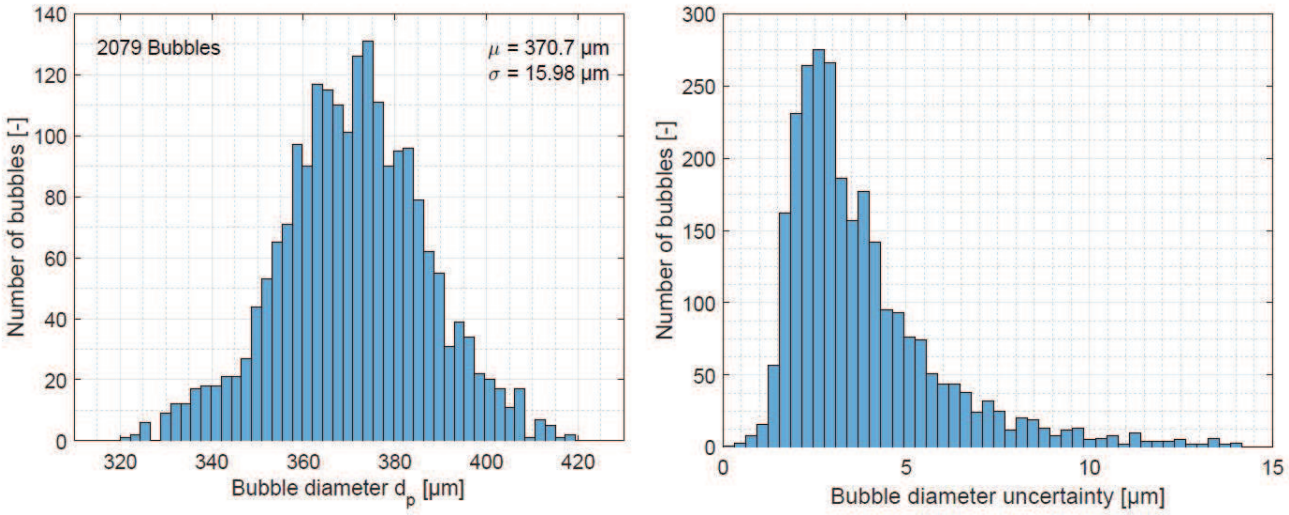

Fig. 6 HFSB diameter statistics. Left: diameter distribution. Right: diameter uncertainty.

Knowing the relaxation time and the bubble diameter, the bubble density can be determined. The density is calculated for each bubble individually, with its own relaxation time and diameter. Figure 7 illustrates the bubble density of each bubble along the stagnation line of the cylinder. In the interval x/ D=[-0.75 -0.65] the mean density value of the HFSBs is found to be 1.18 kg/ m and the standard deviation is measured to be 0.16 kg/ m . The density of air in the laboratory was 1.213 kg/ m^3, giving a specific density $\bar{\rho}$=0.97 ± 0.13.

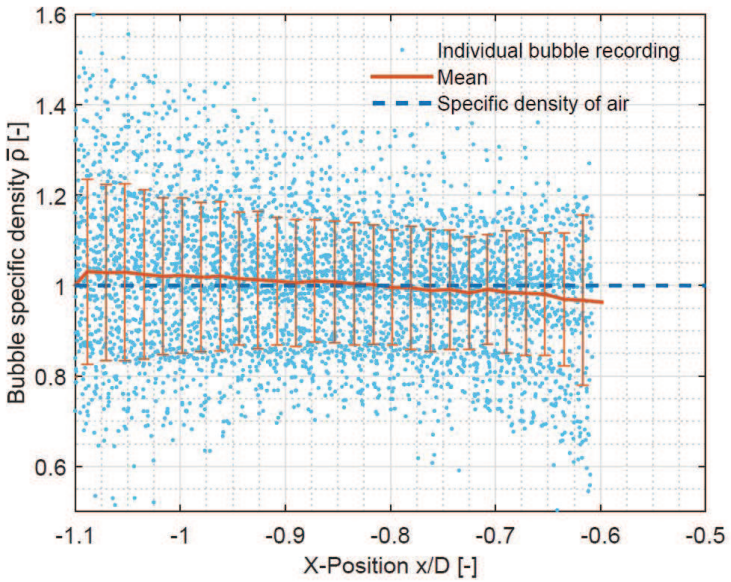

Fig. 7 Bubble density of individual bubbles on the stagnation line of the cylinder for neutrally buoyant helium-filled soap bubbles.

The same approach is applied to helium-filled soap bubbles and air-filled soap bubbles (AFSBs) with different supply flow rates. The results are summarised in Table 1. From the first three combinations a higher ratio q_{bfs}/ q_{He} (i.e. more soap per unit volume helium) increases the density

of the bubble. A higher q_{bfs} also seems to have a stabilizing effect on the dispersion in bubble diameter for a constant flow rate of air. This is visualised in Figure 8-left, where an increase of q_{bfs} results in a lower spread of the bubbles' diameter. At q_{sa}=163 l/ h (HFSB 4 and AFSB 7), an unstable bubble production is reported, which is ascribed to the *jetting* regime. The bubble diameter distribution at this condition is rather broad and non-Gaussian, as illustrated in Figure 8-right for HFSB 4. As a result, the statistical values of bubble diameter and density exhibit a relatively large standard deviation.

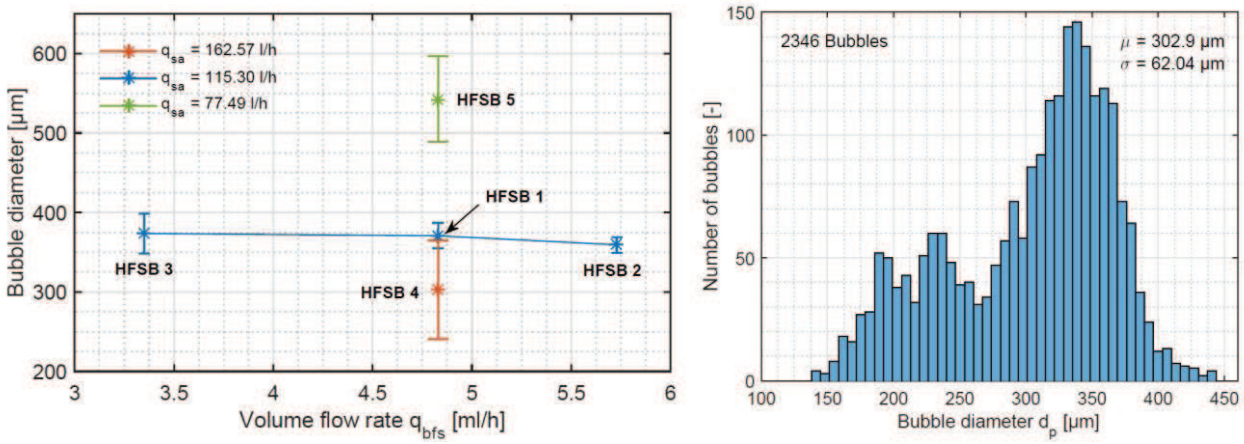

Fig. 8 The influence of the q_{bfs} on the bubble diameter statistics (left) and an example of the unstable bubble production for HFSB 4 (right).

From the diameter observations in HFSB 1 and 2, it is found that the volume flow rate of Helium has a minor effect on the diameter. A higher Helium flow rate will slightly increases the bubble diameter. In case of stable production, a higher volume flow rate of the secondary airflow in the nozzle induces smaller bubbles, while a lower volume flow rate makes the bubbles bigger. This is confirmed by the diameter observations of HFSB 5 and HFSB 4, although the latter has an unstable production. Consequently, the production rate of the bubbles depends on the flow rate of air.

Table. 1 Diameter, relaxation time and density statistics for different helium-filled soap bubbles.

Name	q_{He} [l/h]	q_{bfs} [ml/h]	q_{sa} [l/h]	Diameter [µm]		Relaxation time $\tau_p \cdot \frac{u_{slip}}{\lvert u_{slip} \rvert}$ [µs]		Density ratio $\bar{\rho}$ [-]	
				Mean µ	SD σ	Mean µ	SD σ	Mean µ	SD σ
HFSB 1	4.78	4.83	115.30	370.7	16.0	-6.8	38.9	0.974	0.131
HFSB 2	4.14	5.73	115.30	359.3	9.8	12.8	39.3	1.044	0.141
HFSB 3	4.78	3.35	115.30	373.5	25.1	-44.4	33.7	0.844	0.129
HFSB 4	4.78	4.83	162.57	302.9	62.0	-24.6	32.5	0.931	0.191
HSFB 5	4.78	4.83	77.49	542.6	54.0	-39.6	51.5	0.915	0.123
AFSB 6	5.23	4.83	115.30	437.2	23.7	98.1	37.3	1.304	0.148
AFSB 7	5.23	4.83	162.57	365.3	72.4	87.7	38.4	1.320	0.237
AFSB 8	3.79	4.83	77.49	549.3	11.3	193.0	42.2	1.532	0.164

5. Conclusion

This work presents a statistical characterization of the tracing fidelity of HFSBs for PIV experiments. High-speed visualizations identify two different operating regimes of the bubble generator. In the *bubbling* regime, HFSBs are produced in a stable way and the bubbles' properties are rather monodispersed. Conversely, the *jetting* regime is unstable with a broad distribution of the bubble diameter. The latter is measured independently from the distance of the glare points of individual bubbles. The relaxation time was calculated experimentally for the bubbles along the stagnation line of a cylinder. Through measurements of the relaxation time and the bubbles' diameter, the density of HFSBs was computed. Both stable and unstable production regimes were detected in the results. When the bubble generators operate in a stable production regime, variations of the bubble diameter below 5% are observed. For neutrally buoyant bubbles, the mean value of the relaxation time is of the order of 10 μs, which agrees well with the previous results of Scarano et al. (2015). However, even in these conditions, the standard deviation of the relaxation time exceeds 30 μs. When the bubbles' production regime is unstable, the standard deviation of the bubble diameter and relaxation time can be as high as 70 μm and 50 μs, respectively. These results indicate that the current bubble production systems yield HFSBs allowing accurate measurements of the time-averaged velocity field. Conversely, caution should be taken concerning the accuracy of the instantaneous and fluctuating flow properties, which are directly linked to the spread of the relaxation time of individual bubbles and strongly depends upon the time scales of the specific flow that is investigated.

Acknowledgement

Jan Schneiders is acknowledged for supporting the particle tracking velocimetry analysis.
LaVision GmbH is kindly acknowledged for providing the HFSB generation system.

Bibliography

- Bosbach J, Kühn M, Wagner C (2009) Large scale particle image velocimetry with helium filled soap bubbles. Exp Fluids 14: 2719-2737
- Caridi GCA, Ragni D, Sciacchitano A, Scarano F (2015) A seeding system for large-scale tomographic PIV in aerodynamics. P 11th Int Symp PIV, 14-16 September, Santa Barbara, USA
- Clift R, Grace JR, Weber ME (1978) Bubbles, drops and particles. Academic Press, New York, USA

- Elsinga G, Scarano F, Wieneke B, van Oudheusden B (2006) Tomographic particle image velocimetry. Exp Fluids 41:933-947
- Gañán-Calvo AM, Herrada MA, Garstecki P (2006) Bubbling in unbounded coflowing liquids. Phys Rev Lett 96(12):124504
- Kerho M, Bragg M (1994) Neutrally buoyant bubbles used as flow tracers in air. Exp Fluids 16:393-400
- Kuhn M, Ehrenfried K, Bosbach J, Wagner C (2011) Large-scale tomographic particle image velocimetry using helium-filled soap bubbles. Exp Fluids 50:929-948
- Malik N, Dracos T, Papantoniou D (1993) Particle tracking velocimetry in three-dimensional flows. Exp Fluids 15:279-294
- Mei R (1996) Velocity fidelity of flow tracer particles. Exp Fluids 22:1-13
- Melling A (1997) Tracer particles and seeding for particle image velocimetry. Meas Sci Technol 8(12):1406
- Scarano F (2013) Tomographic PIV: principles and practice. Meas Sci Technol 24(1):012001
- Scarano F, Ghaemi S, Caridi GCA, Bosbach J, Dierksheide U (2015) On the use of helium-filled soap bubbles for large-scale tomographic PIV in wind tunnel experiments. Exp Fluids 56:42
- Schiller L, Naumann A (1933) Über die gundlegenden Berechungen bei der Schwerkraftaufbereitung. Zeitsch Ver Dtsch Ing 77:318-320
- Schneiders JFG, Caridi GCA, Sciacchitano A, Scarano F (2015) Instantaneous pressure measurements from large-scale tomo-PTV with HFSB tracers past a surface-mounted finite cylinder. P AIAA Scitech Conf 2016, 4-8 January 2016, San Diego, California, USA
- Sevilla A, Gordillo JM, Martinez-Bazan, C (2005a) Bubble formation in a coflowing air-water stream. J Fluid Mech 530:181-196
- Sevilla A, Gordillo JM, Martínez-Bazán C (2005b) Transition from bubbling to jetting in a coaxial air–water jet. Phys Fluids 17(1):018105
- van de Hulst H, Wang R (1992) Glare points. Appl Opt 30:4755-4763

PLIF/PIV APPLICATIONS

Application of high-speed PIV and Toluene PLIF techniques to study aerodynamics and thermal stratification inside a flat piston Rapid Compression Machine
M. Ben Houidi, J. Sotton, A. Claverie, C. Strozzi, M. Bellenoue

Analysis of scalar mixing and turbulent flow in a continuous stirred tank by simultaneous PIV and PLIF
M. Marino, A. Busciglio, G. Montante, A. Paglianti

Characterization of High Pressure Natural Gas Injections for Stratified Operation of a Spark Ignited Engine by Simultaneous Fuel Concentration and Air Entrainment Measurements
W. Friedrich, R. Grzeszik, M. Helmich, T. Bossmeyer, M. Wensing

TALIF measurements of atomic oxygen density in L2K plasma wind tunnel
G. Ceglia, A. Del Vecchio, U. Koch, A. Guelhan

Instantaneous temperature imaging by planar laser-induced fluorescence: effect of high laser irradiance
W. Chaze, O. Caballina, G. Castanet, F. Lemoine

Simultaneous 2-Tracer-LIF and PIV for the study of mass transfer around single CO2-bubbles
P. Kováts, K. Zähringer

Laser Induced Fluorescence and Particle Image Velocimetry for the investigation of large-scale structures in turbulent Rayleigh-Bénard convection with high aspect ratio
C. Kästner, M. Körner, A. Kolchynska, C. Resagk

Experimental investigation of the effects of nanosecond repetitive pulsed discharges (NRP) on ignition of methane-air mixtures
A. Seydou, A. Claverie, J. Sotton, M. Bellenoue

Determination of two-dimensional soot particle size by gated laser-induced incandescence and flame temperature measurement
J. Wu, L. Chen, M. Yan, X. Wu, G. Gréhan, K. Cen

Macroscopic Mixing Investigation in a Compressible Accelerated Nozzle Flow using Toluene Tracer LIF
J. Richter, M. Beuting, C. Schulz, T. Dreier, B. Weigand

Development of LIF techniques applied to gas-liquid annular flows
I. Zadrazil, J.S. An, A. Cherdantsev, C.N. Markides